



Cite this: DOI: 10.1039/d4nj00768a

Metal organic framework coated vesicular nano-aggregates: an intelligent 'vehicle' for sustained and leakage proof release of doxorubicin†

Hiral Ukani,^a Bhagyesh Parmar,^a Nildhara Parsana,^a Sugam Kumar,^{id b}
Vinod K Aswal,^{id b} Omar El Seoud^c and Naved Malek^{id *ac}

Designing 'smart' nano carriers with high drug loading capacities and stimuli-responsive drug release behavior is crucial as they boost therapeutic efficiency while reducing side effects in patients and thereby ameliorate the limitations of traditional drug carriers. In this study, we created a ZIF-8 coated pH-responsive catanionic vesicular nano-aggregated drug delivery platform with high doxorubicin (DOX) loading capacity. The vesicular nano-aggregates were designed through synergistic interaction between the bile salt, sodium deoxycholate (NaDC), with a biocompatible ester-functionalized ionic liquid-based surfactant (ILBS), 4-methyl-4-(2-(dodecyloxy)carbonylmethyl)morpholin-4-ium bromide (C₁₂EMorphBr). A composited drug nano-carrier was produced by coating zeolitic imidazolate framework (ZIF-8) on the surface of drug-loaded catanionic vesicular nano aggregates (DOX loaded NaDC/C₁₂EMorphBr@ZIF-8). The study demonstrates that the ZIF-8 shell, as opposed to the catanionic vesicular system, prevents DOX leakage from the core-shell nanocomposites in response to acidic stimulation. The size of these nanocomposites was characterized using DLS, while their morphology and crystallography were examined using SEM, EDS, and XRD. These comprehensive characterizations solidify the DOX-loaded nanocomposite's integrity, affirming the successful coating of ZIF-8 on the surface of the vesicles (NaDC/C₁₂EMorphBr). The DOX loaded NaDC/C₁₂EMorphBr@ZIF-8 nanocomposites effectively prevented DOX leakage and early release, resulting in targeted drug delivery to the intended site. Furthermore, The DOX-loaded nanocomposite was effective in killing MCF-07 cells, with an IC₅₀ value of 4.35 ± 0.5 µg ml⁻¹. This effort aims to maximize the combined and independent performance of the vesicular system and coated nanocomposites.

Received 16th February 2024,
Accepted 11th May 2024

DOI: 10.1039/d4nj00768a

rsc.li/njc

1. Introduction

Cancer, a global health challenge with nearly 10 million deaths in 2020, necessitates improved treatment.¹ While surgical resection is still a key therapeutic strategy, the risk of local cancer recurrence following surgery poses a significant risk to prognoses and survival rates of patients. To reduce the chance

of recurrence, adjuvant therapies such as chemotherapy, radiotherapy, and endocrine therapy are frequently used.^{2,3} However, severe toxicity and systemic adverse effects are frequently associated with these therapies.^{3,4} In light of these challenges, the strategy of localized therapy has gained considerable attention in the field of cancer treatment. This approach presents distinct advantages over conventional therapies, as it allows for targeted delivery of therapeutic drugs to tumor sites, facilitates controlled and sustained release of drug molecules, and minimizes nonspecific distribution in healthy tissues.^{5,6} In recent times, various drug carriers including liposomes, niosomes, solid lipid nanoparticles, polymeric micelles, dendrimers, nanotubes, and magnetic nanoparticles have attracted attention as vehicles for site-specific drug delivery.⁷⁻¹¹ These systems can significantly lower the required drug dosage for effective treatment, thus enhancing therapeutic outcomes.¹²⁻¹⁴ Furthermore, the problems such as poor water solubility and poor stability of drugs should be overcome by building a new drug delivery system that can address the shortcomings of the

^a Ionic Liquids Research laboratory, Department of Chemistry, Sardar Vallabhbhai National Institute of Technology, Surat-07, India.

E-mail: navedmalek@chem.svnit.ac.in

^b Solid State Physics Division, Bhabha Atomic Research Centre, Trombay, Mumbai-400085, India

^c Institute of Chemistry, University of São Paulo, 05508-000 São Paulo, SP, Brazil

† Electronic supplementary information (ESI) available: Results of the catanionic vesicles and ZIF coated composites (turbidity, visual images, normalized absorbance plot, steady state fluorescence data, DLS data, TEM images, EDS analysis) are given as ESI. Stability of the vesicles and ZIF coated composites as a function of temperature, dilution, and pH are also given as ESI. Kinetic model fittings for the drugs loaded within the vesicles and ZIF-coated composites are available as ESI. See DOI: <https://doi.org/10.1039/d4nj00768a>

existing system. Recently designed new age drug delivery vehicles such as surfactants with ionic liquid character, also known as ionic liquid-based surfactants (ILBSs), can be an excellent choice for this.^{15,16} ILBSs are a new class of additives that offer fine-tunable properties with designable nanoaggregates like micelles, vesicles and hydrogels to carry the drug molecules irrespective of their shape, size, charge and polarity.^{17–20} Additionally, ILBSs offer drug stability during circulation, stimuli responsiveness, drug solubility, drug stability and minimal toxicity.

Leveraging their excellent fine-tunable surface-active properties and ability to form various nanoaggregated structures, various ILBSs have been recently tested as new-age drug delivery vehicles either in their purest form or through their synergistic interaction with other additives.^{8,21–23} Although recently studied extensively, ILBS-based drug delivery vehicles face challenges such as limited drug loading capacity and premature drug release and leakage at physiological conditions.^{15,17,24} These limitations can be addressed by coating them with different materials such as polymeric membranes, nanoparticles and very recently through metal–organic frameworks (MOFs).^{25–28} These coated vehicles facilitate not only drug release to the target site without premature release but also improve the drug loading ability of the system and enhance its stability against body fluid. Among these, MOFs have emerged as the most promising coating materials, due to their excellent biosafety, structural tunability, and intracellular absorption capabilities.²⁹ For instance, Yu *et al.* reported an innovative approach to form hollow nanoworms through the growth of MOF nano-crystals on BCP (Block copolymer) micelles.³⁰ Likewise, Lei *et al.* developed BCP@ZIF-8 nanocomposites by growing ZIF-8 nanocrystals on polymeric aggregates to load and release anticancer drugs under acidic conditions.³¹ Although these systems show pH responsive character, the majority of the drug was released only in 10 hours against the 5 hours without coating and it failed in providing prolonged drug release. Designing a biocompatible drug delivery system with adjustable properties and that responds to the intracellular stimuli (pH) with prolonged drug release time and can restrict premature drug release is still a challenge.³¹

To address the above-mentioned concerns, in the present study, we aim to develop biocompatible and stimuli responsive MOF-coated catanionic vesicles as a smart drug delivery vehicle. These new age drug delivery vehicles showcased high drug loading capacity, excellent thermal stability and premature drug release proof system, unlike the previously designed stimuli-responsive drug delivery vehicles.^{21,30–35} Designing the MOF coated delivery system involves two steps among which the first is the development of stable vesicular nanoaggregates through the synergistic interaction between bile salt (NaDC) and C₁₂EMorphBr. Here, ester functionality within the C₁₂EMorphBr enhances its hydrophilicity, surface activity, and biodegradability.²¹ Whereas NaDC is a well-known biological detergent to lyse cells and solubilize cellular and membrane components. The catanionic vesicles (NaDC/C₁₂EMorphBr) formed were then used to encapsulate the

hydrophobic anti-cancer drug DOX. The drug leakage and premature release of the drug prompted the second step where the drug-loaded NaDC/C₁₂EMorphBr was coated through ZIF-8. This transformation resulted in the formation of DOX-loaded NaDC/C₁₂EMorphBr@ZIF-8 nanocomposites, which effectively prevented DOX leakage and premature release. The reason for choosing ZIF-8 from the library of MOFs is its compatibility with other materials, leading to potential uses in hybrid nanocomposites for controlled drug release,²⁸ because of its unprecedented physicochemical properties such as regular microporous structure, strong thermal stability, low cytotoxicity and pH responsive character to name a few.^{36–42} Furthermore, the pore cavities within ZIF-8 have a diameter of 11.6 Å, with the pore opening size to 3.4 Å that can hold and release the molecules from it on acidic pH response.^{43,44} The hybrid nanocomposite exhibits pH-responsiveness with high drug loading capacity. This breakthrough MOF coated drug-loaded vehicle enables precise delivery of the drug to the intended site without premature release, addressing a critical limitation in drug delivery systems.^{28,31,45,46}

2. Materials, preparations and methods

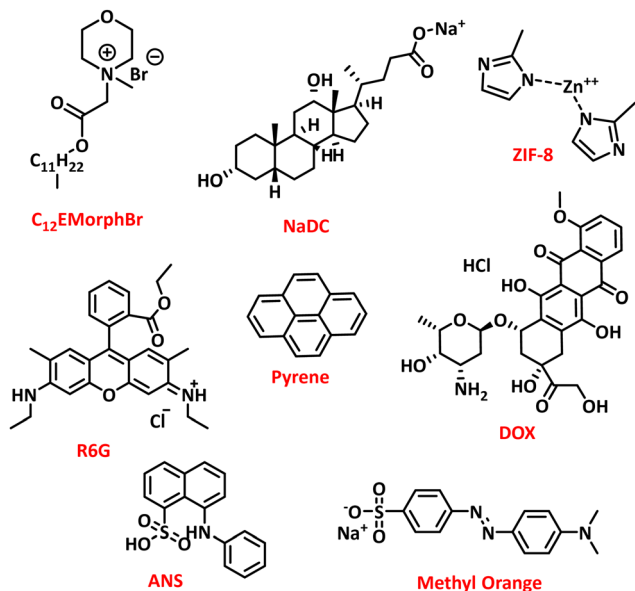
2.1 Materials

N-Methyl morpholine and *p*-toluene sulfonic acid monohydrate were purchased from Sigma Aldrich. Lauryl alcohol was purchased from Merck, while bromoacetic acid was purchased through SRL. C₁₂EMorphBr was synthesized using the method described in our previous research article.⁴⁷ Sodium deoxycholate, zinc nitrate hexahydrate, 2-methyl imidazole, and doxorubicin hydrochloride were purchased from Sigma Aldrich. Rhodamine 6G (R6G), pyrene, 8-anilino-1-naphthalenesulfonic acid (ANS), and methyl orange (MO) were also bought from Sigma Aldrich. Double-distilled Milli-Q water was used for the preparation of solutions. The MCF-07 cell line was purchased from NCCS, while fetal bovine serum and trypsin were purchased from GIBCO. The reagents indicated here were of analytical grade with purities of 99% and were used as received without any additional purification. The molecular structure of individuals is depicted in Scheme 1.

2.2. Preparations

2.2.1. Preparation of solutions (micelle to vesicular). To make C₁₂EMorphBr vesicular solutions with varying sodium deoxycholate (NaDC) content, the appropriate amount of C₁₂EMorphBr (25 mM, 10 times higher than the CMC) was taken. In this solution, different concentrations of NaDC ranging from 1 mM to 10 mM were added. The resulting mixtures were treated with ultrasonic waves from an Oscar Ultrasonic sonicator at 27 °C for 5–8 minutes to induce the formation of NaDC/C₁₂EMorphBr.

2.2.2. Preparation of ZIF-8 coated NaDC/C₁₂EMorphBr. In the pre-prepared NaDC/C₁₂EMorphBr solution (7 mM NaDC/25 mM C₁₂EMorphBr), known quantity of zinc nitrate (Zn(NO₃)₂·6H₂O) was added in solid form. Following that, 2-methyl imidazole

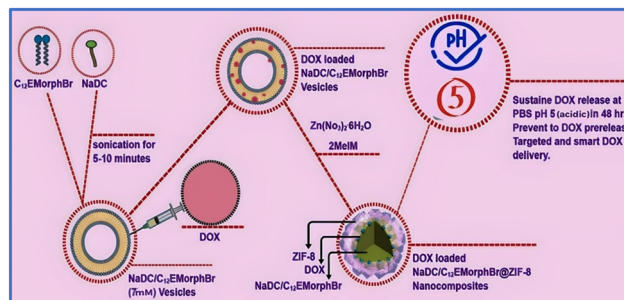


Scheme 1 Molecular composition of the substances utilized in the current investigation.

was added dropwise to the solution, which was then left at room temperature for 3 hours. The resultant product was obtained *via* centrifugation at a rate of 10 000 rpm for 10–15 minutes and washed 3–4 times with deionized water. The solid powder was then acquired by drying the product (NaDC/C₁₂EMorphBr@ZIF-8) in a vacuum oven at 60 °C for 5 hours.

2.2.3. Preparation of DOX-loaded NaDC/C₁₂EMorphBr. Doxorubicin hydrochloride (DOX) powder was added to the NaDC/C₁₂EMorphBr solution and then the solution was allowed to rest for 120 minutes. This will allow the excess DOX (not incorporated within the NaDC/C₁₂EMorphBr) to settle. Subsequently, the solution was centrifuged at 2000 rpm for 5 minutes to eliminate any unbound and insoluble DOX from the vesicular solution. We used absorbance measurement through UV Vis spectroscopy to calculate the DOX loading in NaDC/C₁₂EMorphBr. We observed from comparing the data with the standard calibration curve data that 10.12 mg ml⁻¹ was loaded into the NaDC/C₁₂EMorphBr.

2.2.4. Preparation of DOX-loaded NaDC/C₁₂EMorphBr@ZIF-8 nanocomposites. Firstly, a known quantity of zinc nitrate (Zn(NO₃)₂·6H₂O) was introduced into the DOX-loaded NaDC/C₁₂EMorphBr vesicles (prepared as per Section 2.2.3). Following this, a known quantity of 2-methyl imidazole (2-MeIm) was added drop by drop into the aforementioned solution. The resultant mixture was left at room temperature for a duration of 3 hours. Subsequently, the resulting product was collected through centrifugation (10 000 rpm, 10–15 minutes) and then washed 3 to 4 times with deionized water to remove any unreacted Zn(NO₃)₂·6H₂O and 2-MeIm. Finally, the DOX-loaded NaDC/C₁₂EMorphBr@ZIF-8 nanocomposites were obtained at room temperature with 84.8% loading efficiency of DOX.



Scheme 2 Schematic presentation for the preparation of DOX-loaded NaDC/C₁₂EMorphBr@ZIF-8 nanocomposites.

The loading efficiency (LE) of DOX can be expressed as eqn (1):

$$\text{LE}(\%) = \frac{m(\text{original DOX}) - m(\text{DOX in supernatant})}{m(\text{original DOX})} \times 100 \quad (1)$$

The schematic representation of the preparation of the DOX-loaded NaDC/C₁₂EMorphBr@ZIF-8 nanocomposites is depicted in Scheme 2.

2.2.5. Preparation of ZIF-8. Zinc nitrate (Zn(NO₃)₂·6H₂O) was added in water, after which 2-methyl imidazole was gradually introduced into the solution. The resulting mixture was then allowed to stand at room temperature for 3 hours. Following this, the product was collected through centrifugation at a rate of 10 000 rpm for 10 to 15 minutes, and was subsequently washed 3 to 4 times with deionized water. Finally, the product was dried for 5 hours at 60 °C in a vacuum oven to obtain ZIF-8 powder.

2.3. Methods

2.3.1. Turbidity measurement. An iGENE Lab serve CT-27 spectrophotometer was used throughout the study. Quartz cuvettes with a path length of 1 cm were used. Optical densities for the NaDC/C₁₂EMorphBr in aqueous solution were evaluated with increasing concentration of NaDC. The wavelength used for measuring the optical density was deliberately set at 500 nm, a range where there is negligible absorption of C₁₂EMorphBr.²¹

2.3.2. Dynamic light scattering (DLS) and zeta potential. The Horiba Nano ZS90 (Malvern) was employed to conduct both dynamic light scattering and zeta potential measurements using a He–Ne laser (633 nm, 4 mW). The DLS data were used to calculate the aggregate diameter through the self-regulation method, while the zeta potential measures the electric potential difference between a particle's surface and the surrounding fluid, providing information on the particle's stability and its interaction with other particles or surfaces.

2.3.3. Fluorescence resonance energy transfer (FRET). FRET spectroscopic methods utilize Coulomb interactions facilitated by induced dipole–dipole interactions to transfer energy between an excited donor fluorophore and an acceptor fluorophore. The calculation of the distance between the donor

and acceptor (D–A) is based on Förster's theory, which has also been employed to determine the radius of micelles and the thickness of vesicle bilayers. The donor probe used was ANS (8-anilino-1-naphthalene sulfonic acid), which is hydrophobic, while the acceptor probe, R6G (Rhodamine 6G), is hydrophilic. Both dyes were introduced at consistent micromolar concentrations, and the excitation wavelength was set to 375 nm (λ_{max} of ANS). The efficiency of energy transfer can be expressed as eqn (2),

$$E = \frac{R_0^6}{R_0^6 + R_{\text{DA}}^6} \quad (2)$$

The distance between the molecular centres of D and A is represented by R_{DA} . In the present investigation, the radius of the micelle and the thickness of vesicular aggregation were determined using D and A as hydrophobic and hydrophilic dyes, respectively, which were situated in the inner and outer regions (hydrophobic and hydrophilic regions) of the

$$P(Q) = \frac{16\pi^2}{9} \left[\frac{(R + dR)^3 (\rho_{\text{shell}} - \rho_s) \frac{\sin Q(R + dR) - Q(R + dR) \cos Q(R + dR)}{Q^3 (R + dR)^3}}{-R^3 (\rho_{\text{shell}} - \rho_{\text{core}}) \frac{\sin QR - QR \cos QR}{Q^3 R^3}} \right]^2 \quad (8)$$

aggregates. The distance at which the energy transfer efficiency is deemed to be 50% is known as R_0 , or the Förster distance, which is calculated using the following eqn (3),

$$R_0 = 0.2108 \{k^2 n^{-4} \phi_D J(\lambda)\}^{1/6} \quad (3)$$

The refractive index of the medium is represented by n , while ϕ_D denotes the quantum yield of D in the absence of A. The orientation factor, k^2 (which is usually considered to be 2/3 since the Förster distance has a slight variation across different scenarios), is also included in the equation. The spectral overlap between the emission spectrum of D and the absorption spectrum of A is represented by $J(\lambda)$. The relationship between $J(\lambda)$ and the normalized fluorescence intensity of D ($F_D(\lambda)$) in the absence of A and the extinction coefficient of A (ϵ_A) is described by eqn (4) and (5):

$$J(\lambda) = \int_0^\infty F_D(\lambda) \epsilon_A(\lambda) \lambda^4 d(\lambda) \quad (4)$$

$$R_0^6 = \left[\frac{9000 (\ln 10) k^2 \phi_D}{128 \pi^5 N n^4} \right] \int_0^\infty F_D(\lambda) \epsilon_A(\lambda) \lambda^4 d(\lambda) \quad (5)$$

The efficiency of energy transfer can be determined using the following eqn (6), where F_D denotes the emission intensity of D when A is absent, and F_{DA} represents the emission intensity of D in the presence of A:

$$E = 1 - \frac{F_{\text{DA}}}{F_D} \quad (6)$$

2.3.4. SANS measurement. Small-angle neutron scattering experiments were carried out at the SANS diffractometer located in the Guide Tube Laboratory at Dhruva Reactor, BARC, Mumbai, India. The SANS diffractometer estimates the

coherent differential scattering cross-section per unit volume. A He₃ position sensitive detector is used to track the angular distribution of neutrons scattered by the sample. The Q -range of the instrument ranges from 0.017 to 0.35 Å^{−1}. The experiments were performed at a constant temperature of 30 °C. The experimental data was analysed using the SasView 4.2.0 data fit program, which compares the scattering from various models to the experimental data.²³

Eqn (7) is the ellipsoidal micelles model:

$$I(Q) = \frac{A}{Q^n} + \left[\frac{d \sum(Q)}{d\Omega} \right]^{\text{ellipsoids}} + \text{background} \quad (7)$$

where n is a low- Q Porod exponent, and $[d \sum(Q)/d\Omega]^{\text{ellipsoids}}$ was discussed above the Q -independent background mostly due to incoherent scattering from hydrogen.

The following eqn (8) provides $P(Q)$ for a spherical core-shell structure,

where R is core radius and dR is shell thickness. r_{core} and r_{shell} represent the scattering length densities of the core and shell, respectively.

2.3.5. Computational studies. The data for each molecule were obtained by computing the DFT calculation using the B3LYP method with 6311g+(d,p) set using Gaussian 9W. Also, density reduced gradients (RDG) and iso-surface images were obtained by using MultiWfn Software and VMD, respectively.

2.3.6. Morphological analysis through transmission electron microscopy (TEM), scanning electron microscopy (SEM) and energy dispersive X-ray spectroscopy (EDS). The microstructure of the system was analysed using a JEOL JEM 2100 transmission electron microscope (TEM), which has an accelerating voltage range of 80–200 kV, and a SIGMA 500VP field emission scanning electron microscope with an EDS Sensor was used to determine the morphology of the prepared materials with EDS for investigating the surface morphology and chemical composition of the materials at the micro- and nanoscale.

2.3.7. Crystallographic determination by X-ray diffraction (XRD). The prepared materials were subjected to X-ray diffraction (XRD) analysis using monochromatic Cu-K α (1.54056 Å) radiation and an X-ray diffractometer operating at 40 kV and 30 mA. The XRD measurements were taken in the 2θ range of 5–60°, with a scanning rate of 3° per minute.

2.3.8. Doxorubicin release profile. The DOX release profiles of the DOX-loaded NaDC/C₁₂EMorphBr and DOX loaded NaDC/C₁₂EMorphBr@ZIF-8 nanocomposites were studied at both neutral pH (pH = 7) and acidic pH (pH = 5). To perform the study, DOX-loaded NaDC/C₁₂EMorphBr and DOX loaded nanocomposites were placed in separate dialysis tubes, which were pre-soaked in water for several hours to eliminate preservatives. One dialysis tube each for the DOX-loaded NaDC/C₁₂EMorphBr

and DOX-loaded nanocomposites were kept in beakers with PBS (pH 7) and stirred constantly in a 37 °C water bath, while the other two tubes were placed in another beaker containing PBS (pH 5) with constant stirring and kept in a 37 °C water bath. At regular intervals, a fixed amount of solution was taken from the drug release media and replaced with fresh PBS. The amount of DOX in the release medium was measured by measuring the absorbance of the drug release media at 480–485 nm (λ_{max}) using an iGENE Labeserve CT-27 spectrophotometer.

2.3.9. Cytotoxicity evaluation. An MTT assay “(3-(4,5-dimethylthiazol-2-yl)-2,5-diphenyltetrazolium bromide)” was used to measure *in vitro* cytotoxicity. Human breast cancer cell lines (MCF-07) were cultured in 10% complete media (Fetal bovine serum + Dulbecco’s minimal necessary media) and incubated at 37 °C under humidified conditions until confluency was reached. In summary, cells were put in 96-well plates, cultured for an entire night in an incubator, and then subjected to increasing concentrations of NaDC/C₁₂EMorphBr@ZIF-8 containing DOX (0, 2, 4, 6, 8, 10 and 12 $\mu\text{g mL}^{-1}$). After 24 hours of cultivation, cell viability was calculated through the MTT-assay. Microplate readers were used to measure the absorbance at 570 nm through an Epoch multiplate reader. Experiments were conducted in triplicate for validation.

3. Results and discussion

This article describes a two-stage process aimed at producing durable vesicular nano-aggregates, which are then coated with biocompatible MOF to enable drug delivery application. The first step focuses on the creation of stable vesicular nano-aggregates, while the second step involves applying MOF coatings, particularly ZIF-8, for the purpose of targeted drug delivery. Here a micellar solution of surface-active ionic liquid (C₁₂EMorphBr) was taken that was interacted with the NaDC. Molecular interaction between these two resulted in the transformation of the micellar nano-aggregates of the C₁₂EMorphBr into bigger-sized nanoaggregates, *i.e.*, vesicular nano-aggregates. These vesicular nano-aggregates were characterized by measuring the turbidity and polarity of the system using spectroscopic probes, whereas the size of these nano-aggregates was determined by DLS, SANS, and FRET. The stability of the formed nano-aggregates was further analysed with dilution through spectroscopic probes, and stability with temperature and pH was assessed using DLS. Additionally, the representative vesicular solution was utilized to encapsulate the hydrophobic anti-cancer drug DOX. The drug-loaded NaDC/C₁₂EMorphBr was further examined for drug release under different buffer (PBS) conditions. However, targeted drug release is not possible in this manner, as the leakage and early release of the NaDC/C₁₂EMorphBr limit their usefulness in targeted drug delivery systems. To address this issue, in the second step, the drug loaded NaDC/C₁₂EMorphBr were coated with ZIF-8 to form DOX loaded NaDC/C₁₂EMorphBr@ZIF-8

nanocomposites. The size of these nanocomposites was characterized using DLS, while their morphology and crystallography were examined using SEM, EDS, and XRD. The DOX loaded NaDC/C₁₂EMorphBr@ZIF-8 nanocomposites effectively prevented DOX leakage and early release, resulting in targeted drug delivery to the intended site. Furthermore, cytotoxicity studies were conducted on the MCF-07 breast cancer cell line.

3.1 Characterizing morphological transition

3.1.1. NaDC mediated micelles to the NaDC/C₁₂EMorphBr transition. The objective of the study was to investigate the changes in the microstructure of a mixture of amphiphiles (C₁₂EMorphBr) and (NaDC) in aqueous solution by visual observation and through measuring the turbidity of the solution (Fig. S1 and S2, ESI†). Fig. S1 (ESI†) depicts the changes in absorbance at 500 nm of the amphiphiles with increasing NaDC concentration, which was ten times greater than its CMC. As observed in Fig. S2 (ESI†), the samples were visually clear with almost zero absorbance when the NaDC concentration was low due to the small sized spherical aggregates, SANS results *vide infra*.^{21,48} As the NaDC concentration increased, the absorbance increased steadily until it reached its maximum value, indicating an increase in turbidity because of the larger sized aggregates, may be of NaDC/C₁₂EMorphBr vesicles.^{48,49} However, at a NaDC concentration of 7 mM, the mixture precipitated out, causing a decrease in absorbance (Fig. S2, ESI†).⁵⁰

3.1.2. Analysing the rigidity and hydrophobicity of the aggregates. To investigate the morphological transition, from micellar aggregates to vesicular nano-aggregates, we utilized the solvatochromic azo dye, methyl orange (MO), which is sensitive to the range of medium polarity. A low concentration of MO (20 μM) was used to avoid any interaction with the ILBSs. The occurrence of a hypsochromic shift (blue shift), as observed in Fig. S3 (ESI†), suggests a reduction in polarity with an increase in the NaDC concentration. This shift indicates a possible transformation of the micellar aggregates from relatively polar spherical structures to non-polar vesicular aggregates.²¹ This hydrophobic microenvironment was created by the bilayers of NaDC/C₁₂EMorphBr membranes, indicating the transition from micellar aggregates to vesicular nano-aggregates.^{22,49}

In addition, we utilized pyrene (solvatochromic fluorescence probe) to assess the formation of larger aggregates with lower polarity. Due to its highly hydrophobic nature, pyrene tends to reside in the most hydrophobic regions of the system, such as the core of the micelle and between the bilayers of the NaDC/C₁₂EMorphBr vesicles. The solvatochromic nature of pyrene enables us to determine the polarity of its surrounding microenvironment, where a lower value of I_1/I_3 (ratio of the intensity of the first and third vibronic peaks) indicates a less polar microenvironment around the probe and *vice versa*.²³ By introducing pyrene into the system at various NaDC concentrations, we were able to observe the micellar to vesicular transition in Fig. S4 (ESI†).

3.2. Size and morphology of the nanoaggregates and nanocomposites

Dynamic light scattering (DLS) was utilized to determine the size of various systems, including micellar, vesicular, drug-loaded vesicular, and vesicular nanocomposite systems. The hydrodynamic diameter of the aggregates was estimated using DLS, and the sizes of the aggregates were calculated from the distribution plots presented in Table S1 (ESI†) and Fig. 1. The principle of light scattering theory was applied in DLS, which states that the scattering intensity is proportional to the sixth power of the diameter of the particles or aggregates.⁵¹ According to the data in Table S1 (ESI†), the hydrodynamic diameter of an aqueous solution of C₁₂EMorphBr only (without adding NaDC) was around 17 nm, indicating smaller-sized micellar aggregates. When the NaDC concentration increased to 7.0 mM, the size of the aggregates increased from 17.0 nm to 168.2 nm in the NaDC/C₁₂EMorphBr system. Additionally, the size of the DOX-loaded vesicular aggregates was around 170 nm.

Furthermore, the zeta potential measurements provide important insights into the stability of the aggregates, such as micelles, vesicles, and nanocomposites investigated in this study. The results suggest that surface functionalization has a significant impact on the stability of these particles in suspension, and that the electrostatic repulsion provided by surface charge is an important factor in maintaining stability.^{21,52} And the surface functionalization of the C₁₂EMorphBr (micelles), NaDC/C₁₂EMorphBr (vesicles) and DOX-loaded NaDC/C₁₂EMorphBr@ZIF-8 (nanocomposites) was then investigated by zeta potential measurements. As revealed in Fig. 2, the zeta potential of the DOX, NaDC/C₁₂EMorphBr@ZIF-8 and DOX-loaded NaDC/C₁₂EMorphBr@ZIF-8 was −28.4 mV, 36.1 mV and 13.4 mV, respectively. From the obtained data, the significant change in the zeta potential values of NaDC/C₁₂EMorphBr@ZIF-8 and DOX-loaded NaDC/C₁₂EMorphBr@ZIF-8 suggests the successful encapsulation of the drug in the coated ZIF-8.

Additionally, we utilized SANS and FRET techniques to confirm the results of micellar transition observed in the

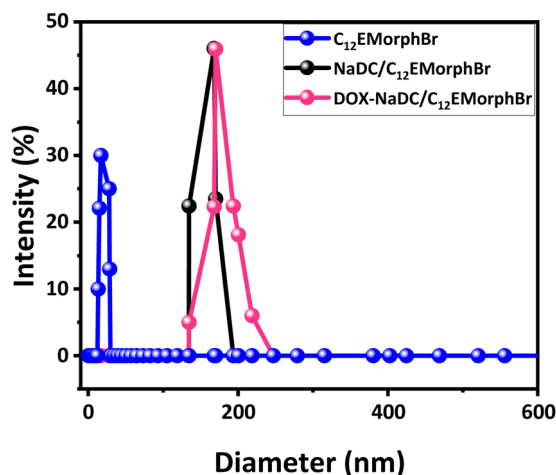


Fig. 1 Size distributions of different systems measured by DLS.

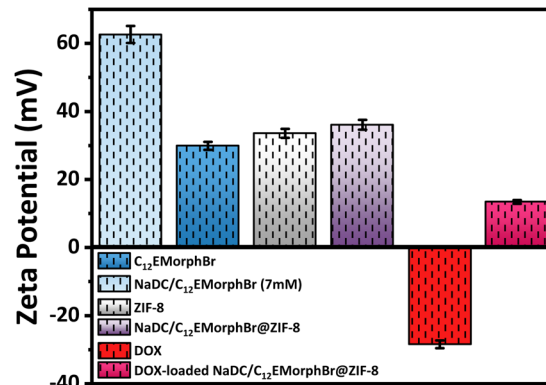


Fig. 2 Zeta potential of different nanoaggregate systems.

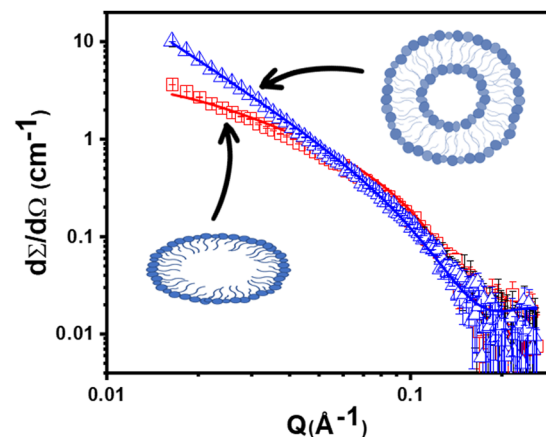


Fig. 3 SANS data of C₁₂EMorphBr at different concentrations of NaDC 2 mM (micelle) and 7 mM (NaDC/C₁₂EMorphBr Vesicle) at 298.15 K.

studied systems. These methods were used to verify the size and structure of the aggregates formed. The SANS scattering results for the NaDC/C₁₂EMorphBr system are presented in Fig. 3 and Table 1. Our observations revealed that C₁₂EMorphBr formed two distinct structural aggregates based on the concentration of NaDC, with micelles formed at 2 mM NaDC and NaDC/C₁₂EMorphBr vesicles at 7.0 mM NaDC concentration. At lower NaDC concentrations, the scattering curves best fitted to the spherically shaped micelle model. As the concentration of NaDC increases, the scattering intensity in the lower *Q* region also increases, indicating the formation of larger aggregates. At a higher concentration of NaDC, *i.e.*, 7 mM, the system showed scattering in the low *Q* region with a slope of −2 on the log-log scale and no correlation peak, indicating the development of NaDC/C₁₂EMorphBr vesicles.²¹

To gain a better understanding of the size and transition of the micelles, we utilized FRET probes to determine the radius of micelles and the bilayer thickness of the vesicles. By using the standard form of Förster theory,^{53,54} we were able to calculate the donor–acceptor separation (*D–A*) in the surfactant-based aggregated system. To investigate micelle size and bilayer thickness, we labelled NaDC/C₁₂EMorphBr micelles

Table 1 Fitted structural parameters of C₁₂EMorphBr at various NaDC concentrations through SANS measurement

[NaDC] mM	Parameters		PDI	Fitted model
2.0	Semi-major axis a (nm) = 17.2	Semi-minor axis b (nm) = 2.2	0.2	Ellipsoidal micelle
7.0	Bilayer thickness R (nm) = 3.1	Core radius R (nm) > 50	0.2	Vesicles

Table 2 Energy transfer parameters for the ANS-R6G pair in the NaDC/C₁₂EMorphBr system at different [NaDC]

[NaDC] mM	1.0 mM	2.0 mM	7.0 mM	8.0 mM
λ_D	483.93	488.03	483.93	483.93
$J(\lambda) \times 10^{-15} \text{ (M}^{-1} \text{ cm}^{-1} \text{ nm}^4\text{)}$	1.97×10^{14}	2.04×10^{14}	1.97×10^{14}	1.97×10^{14}
R_o	28.01823	28.17626	28.01823	28.01823
F_D	96.121	99.56	92.35	113.74
F_{DA}	88.594	91.24	83.68	101.212
E	0.078308	0.083568	0.093882	0.110146
R_{DA}	42.26	42.00	40.88	39.69

$\#J(\lambda) \times 10^{-15} \text{ (M}^{-1} \text{ cm}^{-1} \text{ nm}^4\text{)}$ = spectral overlap between the emission spectrum of D and absorption spectrum of A, λ_D = D's emission wavelength, F_{DA} = intensity of emission of ANS in presence of R6G, F_D = intensity of emission of ANS in absence of R6G, R_{DA} = distance between D and A, R_o = Förster distance (distance between D and A at which the energy transfer efficiency is 50%), E = FRET energy.

and vesicles with the FRET donor–acceptor pair ANS-R6G. The D–A distance, R_{DA} , was calculated using Förster theory and presented in Table 2. The radius of the micelles for the NaDC/C₁₂EMorphBr micelles, which was confirmed by the aforementioned analyses, was determined to be 42.26 Å. These results are consistent with the SANS data presented earlier. On the other hand, at a concentration of 7 mM NaDC, the SANS data showed the presence of vesicles in the system. For the samples containing vesicles, the R_{DA} represents the bilayer thickness, which was determined to be 39.69 Å. These findings also agree with the SANS data discussed previously.

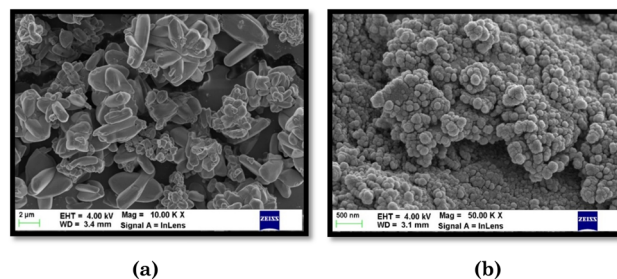
Additionally, in order to gain a more comprehensive understanding of the data, we conducted TEM, and SEM with EDS analysis to examine the morphology, elemental composition and shape of the nanoaggregates and nanocomposites. To begin with, we utilized TEM analysis to examine the nanoaggregates. As shown in Fig. S5(a) (ESI†), the images confirmed the presence of uniformly shaped spherical vesicles of various sizes. In Fig. S5(b) (ESI†), the image displays ZIF-8 coated vesicles, which are spherical in shape due to the NaDC vesicle template. Subsequently, the vesicular aggregates formed by NaDC/C₁₂EMorphBr act as templates, guiding the growth of ZIF-8. Upon introducing measured quantities of Zn²⁺ into the vesicular solutions, Zn²⁺ selectively enriches on the vesicle surfaces due to the strong affinity between N-containing C₁₂EMorphBr and Zn²⁺. Further, the addition of an aqueous mixture of 2-methylimidazole and Zn(NO₃)₂·6H₂O into the vesicular solution demonstrates the growth of ZIF-8 nanocrystals along the surfaces of the assembled structures. A multitude of ZIF-8 particles come together, forming a spherically shaped NaDC/C₁₂EMorphBr@ZIF-8 nanocomposite.

To provide more insight into the characteristics of the nanoaggregate, SEM analysis was employed. After confirming the successful formation of DOX-loaded C₁₂EMorphBr@ZIF-8 nanocomposites that allowed for the creation of nano-carriers with a high drug loading capacity, the self-assembly

morphology of both the DOX-loaded nanocomposite and the pristine ZIF-8 was investigated using SEM. The SEM image in Fig. 4(a) displays the characteristic capsule like morphology of pristine ZIF-8.⁵⁵ Furthermore, Fig. 4(b) illustrates the structural morphology of the DOX-loaded NaDC/C₁₂EMorphBr@ZIF-8 nanocomposites, where the morphology transforms from a capsule to a round, spherical shape. This change can only be explained by the formation of ZIF-8 on the vesicle surface, utilizing vesicles as templates to craft ZIF-8 coated DOX-loaded C₁₂EMorphBr@ZIF-8 nanocomposites.

Furthermore, the chemical composition of the pristine ZIF-8 and DOX-loaded nanocomposites was analysed using EDS, which unveiled their characteristic molecular composition. The EDS spectra shown in Fig. S6 (ESI†) reveal the presence of Zn atoms in both figures, while the intensity of the O atoms increases in Fig. S6(b) (ESI†) due to the larger number of O atoms in DOX.

Furthermore, X-ray diffraction (XRD) analysis was performed to confirm the presence of ZIF-8 crystals in the nanocomposites. The nanocomposite (ZIF-8, NaDC/C₁₂EMorphBr@ZIF-8, DOX-loaded NaDC/C₁₂EMorphBr@ZIF-8) was examined, and its pattern, as shown in Fig. 5, corresponded to the simulated pattern of ZIF-8. The phases identified in the prepared composites,

**Fig. 4** SEM images of (a) neat ZIF-8 and (b) DOX-loaded NaDC/C₁₂EMorphBr@ZIF-8 nanocomposites.

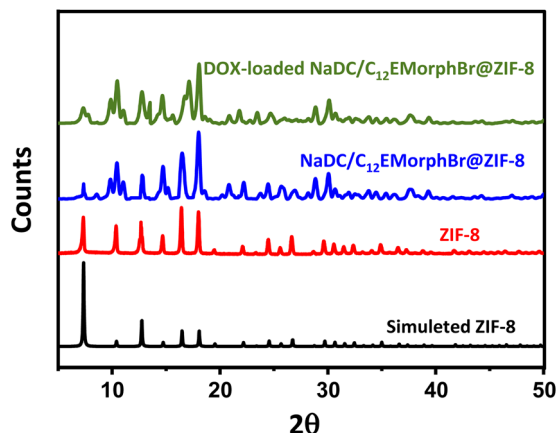
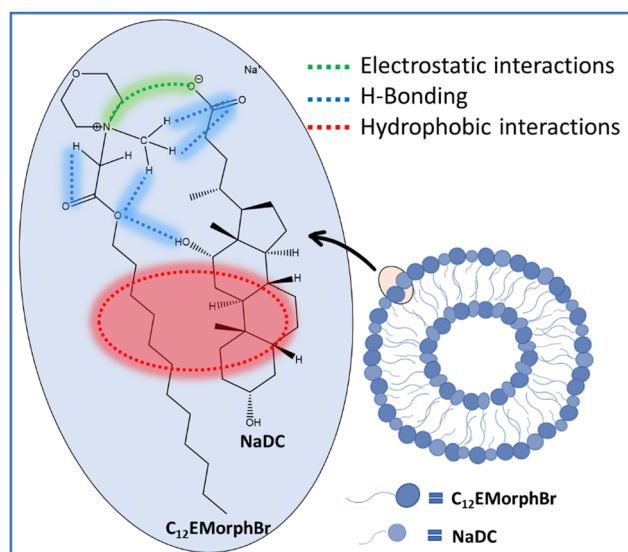


Fig. 5 XRD patterns of the prepared nanocomposites.

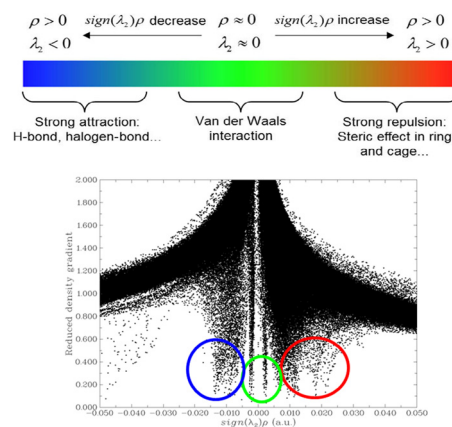
including their respective 2θ values and planes, such as 7.2 (011), 10.35 (002), 12.75 (112), 16.42 (013), and 18.03 (222), were successfully determined for ZIF-8.⁵⁶ The XRD patterns of the DOX-loaded NaDC/C₁₂EMorphBr@ZIF-8 nanocomposite displayed peaks similar to those of the pristine ZIF-8, indicating the successful growth of ZIF-8 on the surface of the NaDC/C₁₂EMorphBr.

3.3. Identifying interaction types

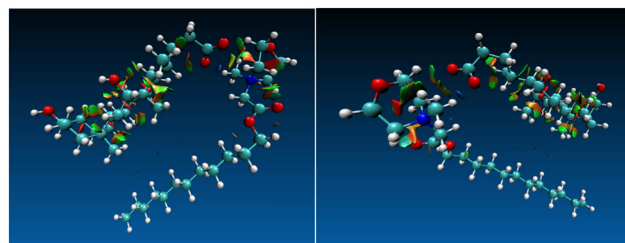
It is crucial to comprehend the interactions responsible for the formation of vesicular nano-aggregates through interacting NaDC and C₁₂EMorphBr. NaDC is a bile salt with a polar group that interacts with the head group of the C₁₂EMorphBr *via* H-bonding and electrostatic interaction, while the non-polar group interacts with the hydrophobic long chain portion of the C₁₂EMorphBr through hydrophobic interaction, resulting in the production of stable vesicular nanoaggregates through



Scheme 3 Possible interactions present on forming NaDC/C₁₂EMorphBr vesicles.



(a)



(b)

Fig. 6 (a) Plots of s versus ρ . These plots were generated by evaluating the DFT B3LYP 6311g+(d,p) set using Gaussian 9W^{61,62} density and reduced gradients on cuboid grids and MultiWfn Software and (b) 3D colour filled RDG iso-surfaces of NaDC/C₁₂EMorphBr vesicles showing the nature of the interaction between the C₁₂EMorphBr and NaDC molecule.

synergistic interaction. A schematic representation of these interactions is shown in Scheme 3.

To confirm the interaction between NaDC and C₁₂EMorphBr, a computational study was conducted. In density functional theory (DFT), the electron density is the crucial quantity from which all chemical properties can be obtained. In order to understand the non-covalent interactions within the vesicles; firstly, the single molecules of NaDC and C₁₂EMorphBr were plotted in Gauss view to optimize them individually, followed by optimization of the vesicular system. After optimizing the individual molecules and system, to analyse non-covalent interactions within C₁₂EMorphBr and NaDC, including van der Waals interaction, hydrogen bonding and steric effects, we have employed a reduced density gradient (RDG) plot, which is derived from the electronic density (ρ) and can be expressed by the following equation.^{57–60}

$$\text{RDG}(r) = \frac{1|\Delta\rho(r)|}{2(3\pi^2)^{\frac{1}{3}}\rho(r)^{\frac{4}{3}}}$$

In the scatter plot (RDG) (Fig. 6(a)), the value of $\text{sign}(\lambda_2)\rho$ being less than zero is an indication of the presence of H-bonding (blue encircled). Similarly, the value of $\text{sign}(\lambda_2)\rho$ displayed at approximately zero (green encircled) and greater than zero (red encircled) is attributed to the van der Waals and steric interactions, respectively. This concept is exemplified in

Fig. 6, where the van der Waals and hydrogen-bonded molecule displays a low and medium-density, gradient spike at negative and at approx zero values, indicating stabilizing interactions present between the morpholinium head group of C₁₂EMorphBr and the –COO[–] group of NaDC. Moreover, the iso-surface image of the system shows the non-covalent interaction with the help of a coloured portion between the molecules. The green, blue, and red colour portion indicates the van der Waals, H-bonding, and steric interactions, respectively (Fig. 6(b)).

As shown in Table 3, the potential energies of NaDC and C₁₂EMorphBr are –1393.188 Hartree and –3601.777 Hartree respectively. These negative values of energy indicate that the molecules are stable in the ground state. When these compounds interact with each other non-covalently and forming a complex, the resultant potential energy of the complex is –4995.512 Hartree. This suggests that the complex formation process is spontaneous and more stable. Furthermore, the binding energy of the complex is calculated to be –0.546 Hartree. These computational findings suggest that one of the responsible factors for the formation of vesicles is the presence of various non-covalent interactions including H-bonding, van der Waals, as well as steric interactions.

3.4. Stability of the nanoaggregates and nanocomposites

To use vesicles and nanocomposites for delivering drugs, it is important to make sure that they remain stable under the physiological conditions. These conditions include body temperature, different levels of dilution, and pH levels. We tested the stability of the NaDC/C₁₂EMorphBr vesicles at different temperatures, dilutions, and pH levels. We also checked how long the NaDC/C₁₂EMorphBr and nanocomposites remain stable over time.

We employed turbidity measurements to track the thermal stability of the NaDC/C₁₂EMorphBr and nanocomposites to determine whether they can be used at body temperature. For NaDC/C₁₂EMorphBr vesicular solutions, since visible light at 500 nm is not absorbed by the vesicle solutions, the turbidity of the solution was determined between 30 °C and 80 °C. Fig. S7(a) (ESI[†]) shows that in the vesicular system, the turbidity of the system made up of the vesicles did not change over the temperature range that was studied, suggesting the stability of the vesicles at the investigated temperature range. Fig. S7(b) (ESI[†]) suggests the size of the hydrodynamic radius of the nanoaggregates as a function of temperature. It shows that in the nanocomposite system, the dynamic radius of the nanocomposites did not change over the temperature range that was

studied, confirming the stability of the studied nanocomposites within the investigated temperature range.

We also tested the dilution stability of vesicular nanoaggregates using spectroscopic probe MO. As stated earlier, in the mixture solution of NaDC/C₁₂EMorphBr (7 mM), the probe experiences the most hydrophobic environment, *i.e.*, that of a solution with higher vesicular aggregates. No shift in λ_{max} was observed after dilution of this vesicular system up to 100 times with Milli Q water (as shown in Fig. S8, ESI[†]), indicating that vesicles are stable on dilution, even after 100 times dilution. In both the NaBut/C₁₂EMorphBr system studied by Jain *et al.* and our previous research on the Cho/C₁₂EMorphBr system, it was observed that stable vesicles were formed even when the solution was significantly diluted. This implies that the vesicular aggregates formed by the ester functionalized morpholinium-based system exhibit robust stability even under conditions of substantial dilution.^{21,47}

We also show that vesicles and nanocomposites have pH stability using DLS-size (hydrodynamic radius) experiments.^{63,64} The size of the NaDC/C₁₂EMorphBr vesicles is stable in the pH range of 4–8; however, above pH 8, the vesicles may breakdown and precipitate out of solution, increasing the size of the solution (Fig. S9(a), ESI[†]). However, in the case of nanocomposites, they are stable at a neutral or basic pH (~7 to 10). However, the size of the aggregates is smaller at lower pH because ZIF-8 is brittle at acidic pH (Fig. S9(b), ESI[†]).⁶⁵ So, DOX loaded NaDC/C₁₂EMorphBr@ZIF-8 nano-aggregates breakdown under acidic conditions, *i.e.*, at pH ≤ 5. Additionally, our data supports this observation by indicating that the surface charge (zeta potential) of the nanocomposite is +13.4 mV at pH 7.0 (neutral) and +19.9 mV at pH 5 (acidic). These positively increased zeta potential values can be attributed to the excess zinc ions present on the particle surface, particularly notable in acidic conditions due to the potential breakdown of ZIF-8.⁶⁶

To ensure the stability of the vesicles and nanocomposites for drug delivery purposes, we conducted DLS experiments to assess their long-term storage stability. We monitored the size and transparency of the materials over an extended period and found that the vesicles and nanocomposites maintained their initial size and transparency even after being stored for more than 6 months at room temperature (Table S2, ESI[†]). This indicates that they exhibit excellent storage stability under normal conditions.

4. Release of anticancer drug in the NaDC/C₁₂EMorphBr and nanocomposites

In our *in vitro* investigation, we opted to use DOX as the drug of choice to determine the potential of the vesicles we created in drug delivery systems. DOX is a well-known and widely utilized anticancer drug that has demonstrated efficacy against various types of cancers. The utilization of vesicles as a drug delivery system has gained popularity in recent times owing to their capacity to protect drugs from degradation, and enhance their

Table 3 Potential energy of C₁₂EMorphBr, NaDC and formed NaDC/C₁₂EMorphBr vesicles

Compound	Potential energy	BE (hartree)	BE (kcal mol ^{–1})
C ₁₂ EMorphBr	–3601.777	—	—
NaDC	–1393.188	—	—
NaDC/C ₁₂ EMorphBr vesicles	–4995.512	–0.546	–342.620

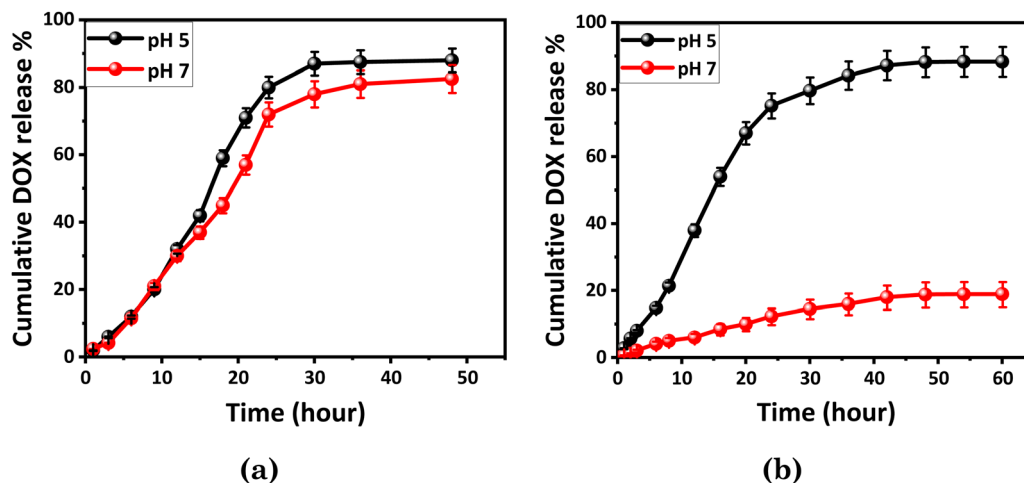


Fig. 7 Doxorubicin % $v s^{-1}$ time with different pH of DOX loaded (a) NaDC/C₁₂EMorphBr vesicles and (b) NaDC/C₁₂EMorphBr@ZIF-8 nanocomposites.

solubility. As a result, our study was focused on investigating the potential of our DOX-loaded NaDC/C₁₂EMorphBr@ZIF-8 nanocomposites in this area, with DOX serving as a model drug for our assessment. To assess the performance of the as-prepared vesicles and nanocomposites for drug delivery, we examined the release kinetics of DOX from the DOX-loaded vesicles and nanocomposites in different pH solutions to verify targeted release. The outcomes demonstrated that DOX was released from the nanocomposites in a pH-dependent manner, with a greater release at lower pH values.

To assess the release behaviour of DOX from the vesicles, the cumulative DOX release was measured, and the highest value of 88% was observed at pH 5.0, as depicted in Fig. 7(a). At pH 7, the drug release was approximately 82.5% after 48 hours, indicating that DOX release from the vesicles was almost the same due to the stability of vesicular aggregates at a broad pH range of 3–8. This suggested that the vesicular nanoaggregates remained stable at different pH values, leading to similar DOX release over time. Furthermore, the cumulative drug release pattern displayed a biphasic nature with an initial burst release, responsible for releasing over $\sim 75\%$ of the DOX in the first 24 hours at pH 5.0 and pH 7.0, as demonstrated in Fig. 7(a). Following the release of DOX into the NaDC/C₁₂EMorphBr vesicles, the solution remains in vesicular form. This is due to the inherent stability of NaDC/C₁₂EMorphBr vesicles within the pH range of 4 to 8 (Fig. S9(a), ESI[†]). Furthermore, post-release, SANS experiments confirm the persistence of the vesicular form (Fig. 8).

Fitted data on kinetic models suggested that the drug release kinetics follows the Ritger–Peppas model (Table S3 and Fig. S10, ESI[†]). However, nanoaggregates present issues such as difficulties in targeting, pre-release at unintended sites, conserving the leakage, and other concerns.³¹ To overcome these challenges, we introduced a coating of ZIF-8 around the vesicles, which prevented pre-release and enabled us to pinpoint the precise location of release, thereby preventing the DOX drug from harming normal cells in the body. This

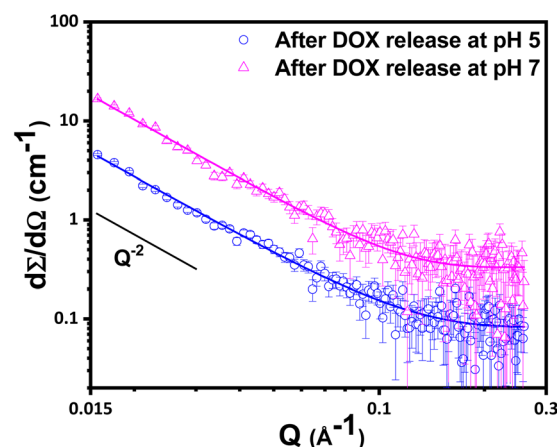


Fig. 8 SANS data of post DOX release from NaDC/C₁₂EMorphBr vesicles.

innovative solution was proposed to improve the effectiveness and safety of drug delivery systems.²⁸

The effect of pH (specifically pH 5.0) on the release of DOX from NaDC/C₁₂EMorphBr@ZIF-8 was studied (Fig. 7(b)). It was found that at a neutral pH of 7, the release of DOX from the nanocomposite was significantly limited with only 18.8% after 48 hours (Fig. 7(b)). This suggested that the ZIF-8 coating functioned as a gatekeeper, hindering the release of DOX from the nanocomposite. Conversely, an acidic environment (pH 5.0) facilitated the release of DOX, with up to 88.2% of DOX being released after 48 hours. The pH-induced disassembly of the interior vesicles led to a gradual disintegration of the ZIF-8 coating.³¹ These changes corresponded well with the drug release behavior, indicating the material's responsiveness to external stimuli. To support our findings, we have compared the DOX loading and release behaviour of some recently studied systems and compiled the data in Table 4. As shown in Table 4, the present system shows the highest drug loading for DOX and exhibits the prolonged drug release of DOX at the

Table 4 DOX loading and release of the presently studied system with the reported systems

System	Drug loading	Drug release		Ref.
		pH 5	pH 7	
EKCEK micelles zwitterionic oligopeptides	44.6%	72 h-50%	~9%	67
HA-g-mPEG-polymer@DOX-1	53.2	20 h-75.13%	20 h-44.12%	68
DOX-NSV6grad	47.93%	72 h-48%	72 h-12%	69
DOX@ZIF-8-FA	15.7%	12 days- 68.8%	12 days-48.5%	70
ZnO-DOX@ZIF-8	11.2%	24 h-80%	24 h-20%	71
DOX-loaded BCP@ZIF-8	33.1%	40 h-80%	40 h-10%	31
DOX-Fe ₃ O ₄ -ZIF-8	12%	—	48 h-89%	72
DOX loaded mPEG-PBLAsp-hyPEI	5.5%	72 h-~48%	72 h-~46%	73
DOX loaded PEG- <i>b</i> -PBCL	8.77%	—	50 h-~58%	74
DOX-loaded NaDC/C ₁₂ EMorphBr@ZIF-8	84.8%	48 h-88.2%	48 h-18.8%	This Work

targeted site, *i.e.* at pH 5.0 as compared to the other reported systems.

The objective was to analyse the DOX release kinetics from NaDC/C₁₂EMorphBr vesicles and NaDC/C₁₂EMorphBr@ZIF-8 nanocomposites by fitting the release data to various models, including the zero order, first order, Higuchi, Hixson–Crowell, Korsmeyer–Peppas and Ritger–Peppas models, and identify the best fit. The R^2 and rate constant values were determined for each model, and the regression analysis was performed for different environments (Table S3, ESI†). In the case of NaDC/C₁₂EMorphBr vesicle systems and their release of DOX, if the experimental data fits well with the Ritger–Peppas model, it suggests that this model adequately describes the release kinetics. The release kinetics of DOX in

the NaDC/C₁₂EMorphBr@ZIF-8 nanocomposites were investigated, and it was observed that the Korsmeyer–Peppas model was the most suitable for describing the data. This model exhibited a strong correlation in various environments. To assess the diffusion mechanism, the Korsmeyer–Peppas model, commonly employed for nanoparticle drug release analysis, was utilized. The release exponent (n) in this model provided valuable insights into the drug release mechanism from the nanoparticles. Notably, the values you provided, $n = 0.7423$ at pH 7 and $n = 1.3160$ at pH 5, indicated distinct release mechanisms under different pH conditions (Table S3, ESI†).

At pH 7, the release exponent value of 0.7423 suggests a non-Fickian or anomalous release mechanism. This suggests that the drug release from the nanoparticles at pH 7 is not solely

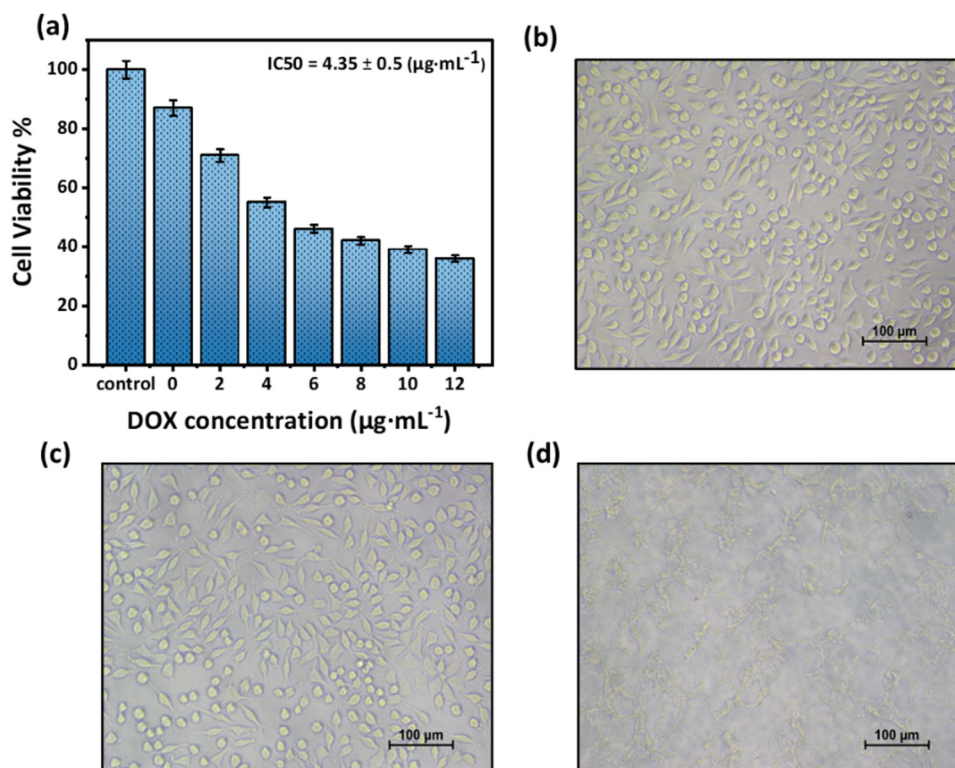


Fig. 9 (a) The percentage of viable MCF-7 cells after treatment, (b) untreated MCF-7 cells, (c) MCF-7 cells treated with NaDC/C₁₂EMorphBr@ZIF-8 and (d) MCF-7 cells treated with NaDC/C₁₂EMorphBr@ZIF-8 loaded with DOX.

controlled by diffusion, but other mechanisms may also be contributing.⁷⁵ Conversely, for pH 5, the release exponent value of 1.3160 implies a release mechanism characterized by super case-II transport or erosion-controlled release. In the case of super case-II transport, the drug release rate surpasses the rate of matrix erosion, leading to an accelerated drug release. Thus, it suggests that at pH 5, the drug release from the nanoparticles is predominantly governed by the erosion or degradation of the matrix.⁷⁵ Kinetics studies of drug release can provide physically significant parameters that can be used for comparison and linking the release parameter to important parameters such as bioavailability.^{76–78}

4.3. Cell line study

To examine the cytotoxicity of ZIF-8 and DOX-loaded nanocomposites, we utilized MCF-7 cell lines. Pristine ZIF-8 shows minimal to no cytotoxicity, whereas the DOX-loaded nanocomposites displayed increased toxicity towards breast cancer cell lines. By using GraphPad Prism software, we were able to calculate the IC₅₀ values for the nanocomposites containing DOX against MCF-7 cell lines. Our results (Fig. 9) indicate the effectiveness of our approach as a drug delivery method. Specifically, after 24-hour exposure, we determined the IC₅₀ values for the nanocomposites containing DOX for MCF-7 cells to be $4.35 \pm 0.5 \mu\text{g mL}^{-1}$. Our results are in accordance with the results reported by Honghui Li *et al.*, who observed that the IC₅₀ value of DOX-loaded MIL-101 MOF nanoparticles on MCF-7 cells was $10 \mu\text{g mL}^{-1}$ after a 24-hour treatment.⁷⁹ Zahra Gharehdaghi *et al.* fabricated copper metal organic framework nanocomposites Fe₃O₄@Cu₃(BTC)₂-DOX. The IC₅₀ value for this system is $6.77 \mu\text{g mL}^{-1}$ after 24-hours.⁸⁰ Ashraf A. El-Bindary *et al.* prepared nanoparticles of ZIF-8 that showed low cytotoxicity, while DOX@ZIF-8 showed high cytotoxicity to HepG-2 and MCF7 cells compared with free DOX at the equivalent concentration of DOX of $>12.5 \mu\text{g mL}^{-1}$.⁸¹ These findings indicate that DOX@ZIF-8 nanoparticles are a promising method for the delivery of cancer cells to drugs.⁸² The complex DOX-ZIF-8 exhibits lower cytotoxicity than pure DOX for the tested cells, possibly due to the slower release of the drug.⁸²

5. Conclusions

As an intelligent drug delivery vehicle, we devised pH responsive NaDC/C₁₂EMorphBr@ZIF-8 nanocomposites, using self-assembled DOX loaded NaDC/C₁₂EMorphBr vesicles as a template for coating ZIF-8 on the surface of the vesicles. The resulting system showed promising thermal and pH stability, and high drug encapsulating ability, which could be one of the important aspects while designing nanocomposites for drug delivery. In particular, the drug was very less released under physiological conditions (PBS, pH 7), but it was released in a controlled manner under acidic conditions (pH 5) with approximately 88.2% efficiency, after being sustainably delivered over a period of 48 hours. This serves as an efficient nanocomposite,

releasing the drug in a stimuli-responsive sustained fashion. The DOX-loaded nanocomposites were effective in killing MCF-7 cells, with an IC₅₀ value of $4.35 \pm 0.5 \mu\text{g mL}^{-1}$. The findings in this work may open a novel approach for the use of IL-MOF Nanocomposite hybrid systems to deliver anticancer drugs, with benefits to the therapy of different diseases and health problems.

Author contributions

Hiral Ukani: conceptualization, methodology, writing – original draft and visualization. Bhagyesh Parmar: conceptualization, methodology, writing – original draft and visualization. Nildhara Parsana: conceptualization, methodology. Sugam Kumar: conceptualization, methodology. Vinod K Aswal: conceptualization, methodology. Omar El Seoud: writing – original draft and visualization. Naved I. Malek: conceptualization, supervision, writing – review and editing, funding acquisition. All authors have given approval to the final version of the manuscript.

Conflicts of interest

There are no conflicts to declare.

Acknowledgements

NM acknowledges the financial assistance of UGC-DAE for the Collaborative Research Scheme (UDCSR/MUM/AO/CRS-M-997/2023). The authors are thankful to Dr Arvind Kumar (CSMCRI, India) for the XRD and TEM analysis and also for the useful discussion.

References

- 1 H. Sung, J. Ferlay, R. L. Siegel, M. Laversanne, I. Soerjomataram, A. Jemal and F. Bray, *Ca-Cancer J. Clin.*, 2021, **71**, 209–249.
- 2 D. A. Mahvi, R. Liu, M. W. Grinstaff, Y. L. Colson and C. P. Raut, *Ca-Cancer J. Clin.*, 2018, **68**, 488–505.
- 3 U. Anand, A. Dey, A. K. S. Chandel, R. Sanyal, A. Mishra, D. K. Pandey, V. De Falco, A. Upadhyay, R. Kandimalla, A. Chaudhary, J. K. Dhanjal, S. Dewanjee, J. Vallamkondu and J. M. Pérez de la Lastra, *Genes Dis.*, 2023, **10**, 1367–1401.
- 4 V. Zanusso, V. Fregoni and L. Gervaso, *Future Sci. OA*, 2020, FSO617.
- 5 Z. Edis, J. Wang, M. K. Waqas, M. Ijaz and M. Ijaz, *Int. J. Nanomed.*, 2021, **16**, 1313–1330.
- 6 S. Senapati, A. K. Mahanta, S. Kumar and P. Maiti, *Signal Transduction Targeted Ther.*, 2018, **3**, 7.
- 7 S. Paul, S. Mukherjee and P. Banerjee, *Mater. Adv.*, 2023, **4**, 2042–2061.
- 8 Z. S. Vaid, A. Kumar, O. A. El Seoud and N. I. Malek, *RSC Adv.*, 2017, **7**, 3861–3869.

- 9 S. M. Rajput, S. Kumar, V. K. Aswal, O. A. El Seoud, N. I. Malek and S. K. Kailasa, *ChemPhysChem*, 2018, **19**, 865–872.
- 10 J. A. Borm and D. Jong, *Int. J. Nanomed.*, 2008, **3**, 133–149.
- 11 S. Su and P. M. Kang, *Pharmaceutics*, 2020, **12**, 837.
- 12 Y. Lu, E. Zhang, J. Yang and Z. Cao, *Nano Res.*, 2018, **11**, 4985–4998.
- 13 P. Liu, G. Chen and J. Zhang, *Molecules*, 2022, **27**, 1372.
- 14 J. Liu, H. Lee and C. Allen, *Curr. Pharm. Des.*, 2006, **12**, 4685–4701.
- 15 R. M. Moshikur, Md. K. Ali, M. Moniruzzaman and M. Goto, *Curr. Opin. Colloid Interface Sci.*, 2021, **56**, 101515.
- 16 A. Shah, M. Kuddushi, S. Rajput, O. A. El Seoud and N. I. Malek, *ACS Omega*, 2018, **3**, 17751–17761.
- 17 C. S. Buettner, A. Cognigni, C. Schröder and K. Bica-Schröder, *J. Mol. Liq.*, 2022, **347**, 118160.
- 18 O. A. el Seoud, N. Keppeler, N. I. Malek and P. D. Galgano, *Polymers*, 2021, **13**, 1100.
- 19 N. Parsana, H. Ukani, O. A. El Seoud, A. Al-Ghamdi and N. Malek, *Chem. Eng. J.*, 2024, **488**, 150703.
- 20 N. Parsana, H. Ukani, D. S. Chauhan, O. El Seoud, S. Mehra, A. Kumar, N. Raje and N. Malek, *RSC Pharm.*, 2024, DOI: [10.1039/D3PM00088E](https://doi.org/10.1039/D3PM00088E).
- 21 M. Jain, A. Marfatia, N. Imam, D. Ray, V. K. Aswal, N. Y. Patel, V. H. Raval, S. K. Kailasa and N. I. Malek, *J. Mol. Liq.*, 2021, **341**, 117396.
- 22 S. M. Rajput, K. Mondal, M. Kuddushi, M. Jain, D. Ray, V. K. Aswal and N. I. Malek, *Colloid Interface Sci. Commun.*, 2020, **37**, 100273.
- 23 M. Jain, S. Kumar, V. K. Aswal, A. Al-Ghamdi, S. Kumar Kailasa and N. I. Malek, *J. Mol. Liq.*, 2022, **360**, 119517.
- 24 S. N. Pedro, C. S. R. Freire, A. J. D. Silvestre and M. G. Freire, *Encyclopedia*, 2021, **1**, 324–339.
- 25 E. Ranjbari, M. R. Hadjmohammadi, F. Kiekens and K. De Wael, *Anal. Chem.*, 2015, **87**, 7894–7901.
- 26 Y. Ohya, S. Takeda, Y. Shibata, T. Ouchi and A. Maruyama, *Macromol. Chem. Phys.*, 2010, **211**, 1750–1756.
- 27 Y. Ohya, S. Takeda, Y. Shibata, T. Ouchi, A. Kano, T. Iwata, S. Mochizuki, Y. Taniwaki and A. Maruyama, *J. Controlled Release*, 2011, **155**, 104–110.
- 28 Y. Jiang, Z. Lei and Z. Tong, *Front. Mater. Sci.*, 2022, **16**, 220600.
- 29 S. Mallakpour, E. Nikkhoo and C. M. Hussain, *Coord. Chem. Rev.*, 2022, **451**, 214262.
- 30 H. Yu, X. Qiu, P. Neelakanda, L. Deng, N. M. Khashab, S. P. Nunes and K.-V. Peinemann, *Sci. Rep.*, 2015, **5**, 15275.
- 31 Z. Lei, Q. Tang, Y. Ju, Y. Lin, X. Bai, H. Luo and Z. Tong, *J. Biomater. Sci., Polym. Ed.*, 2020, **31**, 695–711.
- 32 M. Kuddushi, S. Rajput, A. Shah, J. Mata, V. K. Aswal, O. El Seoud, A. Kumar and N. I. Malek, *ACS Appl. Mater. Interfaces*, 2019, **11**, 19572–19583.
- 33 R. Pansuriya, T. Patel, S. Mehra, A. Kumar, O. A. El Seoud, S. Kumar, V. K. Aswal, S. K. Kailasa and N. I. Malek, *New J. Chem.*, 2023, **47**, 14261–14272.
- 34 T. Patel, R. Pansuriya, S. Mehra, A. Kumar, O. El Seoud, M. A. Assiri and N. Malek, *J. Mol. Liq.*, 2023, **391**, 123099.
- 35 M. Jain, O. El Seoud, S. K. Kailasa and N. I. Malek, *J. Ionic Liq.*, 2022, **2**, 100046.
- 36 R. Ettlinger, N. Moreno, D. Volkmer, K. Kerl and H. Bunzen, *Chem. – Eur. J.*, 2019, **25**, 13189–13196.
- 37 X. Lian, Y. Fang, E. Joseph, Q. Wang, J. Li, S. Banerjee, C. Lollar, X. Wang and H.-C. Zhou, *Chem. Soc. Rev.*, 2017, **46**, 3386–3401.
- 38 J. I. Brauman, *Science*, 1992, **255**, 1049.
- 39 M.-X. Wu and Y.-W. Yang, *Adv. Mater.*, 2017, **29**, 1606134.
- 40 S. Cao, G. Gody, W. Zhao, S. Perrier, X. Peng, C. Ducati, D. Zhao and A. K. Cheetham, *Chem. Sci.*, 2013, **4**, 3573.
- 41 H. Huang, J.-R. Li, K. Wang, T. Han, M. Tong, L. Li, Y. Xie, Q. Yang, D. Liu and C. Zhong, *Nat. Commun.*, 2015, **6**, 8847.
- 42 H. Zheng, Y. Zhang, L. Liu, W. Wan, P. Guo, A. M. Nyström and X. Zou, *J. Am. Chem. Soc.*, 2016, **138**, 962–968.
- 43 Z. Lu, C. B. Knobler, H. Furukawa, B. Wang, G. Liu and O. M. Yaghi, *J. Am. Chem. Soc.*, 2009, **131**, 12532–12533.
- 44 R. Banerjee, H. Furukawa, D. Britt, C. Knobler, M. O’Keeffe and O. M. Yaghi, *J. Am. Chem. Soc.*, 2009, **131**, 3875–3877.
- 45 J. Bi, Y. Lu, Y. Dong and P. Gao, *J. Nanomater.*, 2018, **2018**, 1–5.
- 46 C. Zheng, Y. Wang, S. Z. F. Phua, W. Q. Lim and Y. Zhao, *ACS Biomater. Sci. Eng.*, 2017, **3**, 2223–2229.
- 47 H. Ukani, Pratyush, S. Kumar, V. K. Aswal, A. A. Al-Ghamdi and N. I. Malek, *ChemistrySelect*, 2022, **7**, e202201613.
- 48 S. M. Rajput, K. Gangele, K. M. Poluri, D. Ray, V. K. Aswal, S. K. Kailasa and N. I. Malek, *Colloids Interface Sci. Commun.*, 2021, **44**, 100466.
- 49 Z. S. Vaid, S. M. Rajput, M. Kuddushi, A. Kumar, O. A. El Seoud and N. I. Malek, *ChemistrySelect*, 2018, **3**, 1300–1308.
- 50 J. D. Jang, C. Do, J. Bang, Y. S. Han and T.-H. Kim, *Polymers*, 2019, **11**, 63.
- 51 J. Lim, S. P. Yeap, H. X. Che and S. C. Low, *Nanoscale Res. Lett.*, 2013, **8**, 381.
- 52 V. Ayala, A. P. Herrera, M. Latorre-Esteves, M. Torres-Lugo and C. Rinaldi, *J. Nanopart. Res.*, 2013, **15**, 1874.
- 53 J. Lv, W. Qiao and Z. Li, *Colloids Surf., B*, 2016, **146**, 523–531.
- 54 C. Ghatak, V. G. Rao, S. Mandal, R. Pramanik, S. Sarkar, P. K. Verma and N. Sarkar, *Spectrochim. Acta, Part A*, 2012, **89**, 67–73.
- 55 A. Deacon, L. Briquet, M. Malankowska, F. Massingberd-Mundy, S. Rudić, T. L. Hyde, H. Cavaye, J. Coronas, S. Poulston and T. Johnson, *Commun. Chem.*, 2022, **5**, 18.
- 56 S. Mehra, V. Poliseti, K. Damarla, P. Ray and A. Kumar, *ACS Appl. Mater. Interfaces*, 2021, **13**, 41249–41261.
- 57 P. Hohenberg and W. Kohn, *Phys. Rev.*, 1964, **136**, B864–B871.
- 58 A. D. Becke, Exchange-Correlation Approximations in Density-Functional Theory, in *Modern Electronic Structure Theory: Part II*, ed. D. R. Yarkony, Johns Hopkins Univ., USA, 1995, pp. 1022–1046.
- 59 A. J. Cohen, P. Mori-Sánchez and W. Yang, *Science*, 2008, **321**, 792–794.
- 60 G. v Gibbs, D. F. Cox and K. M. Rosso, *J. Phys. Chem. A*, 2004, **108**, 7643–7645.

- 61 A. D. Becke, *J. Chem. Phys.*, 1993, **98**, 5648–5652.
- 62 C. Lee, W. Yang and R. G. Parr, *Phys. Rev. B: Condens. Matter Mater. Phys.*, 1988, **37**, 785–789.
- 63 R. Chang, Y. Tian, Y. Wang and J. Qin, *Nanomater. Nanotechnol.*, 2016, **6**, 6.
- 64 J. Du and S. P. Armes, *J. Am. Chem. Soc.*, 2005, **127**, 12800–12801.
- 65 K. Leus, T. Bogaerts, J. De Decker, H. Depauw, K. Hendrickx, H. Vrielinck, V. Van Speybroeck and P. Van Der Voort, *Microporous Mesoporous Mater.*, 2016, **226**, 110–116.
- 66 A. Mittal, S. Gandhi and I. Roy, *Sci. Rep.*, 2022, **12**, 10331.
- 67 W. Xue, A. Trital, S. Liu and L. Xu, *New J. Chem.*, 2020, **44**, 12633–12638.
- 68 B. Lu, Y. Li, Z. Wang, B. Wang, X. Pan, W. Zhao, X. Ma and J. Zhang, *New J. Chem.*, 2019, **43**, 12275–12282.
- 69 M. Di Francesco, C. Celia, M. C. Cristiano, N. d'Avanzo, B. Ruozzi, C. Mircioiu, D. Cosco, L. Di Marzio and M. Fresta, *ACS Omega*, 2021, **6**, 2973–2989.
- 70 J. Bi, Y. Lu, Y. Dong and P. Gao, *J. Nanomater.*, 2018, **2018**, 1–5.
- 71 C. Zheng, Y. Wang, S. Z. F. Phua, W. Q. Lim and Y. Zhao, *ACS Biomater. Sci. Eng.*, 2017, **3**, 2223–2229.
- 72 C. Cheng, C. Li, X. Zhu, W. Han, J. Li and Y. Lv, *J. Biomater. Appl.*, 2019, **33**, 1373–1381.
- 73 H. Feng, D. Chu, Z. Li, Z. Guo, L. Jin, B. Fan, J. Zhang and J. Li, *RSC Adv.*, 2018, **8**, 25949–25954.
- 74 K. E. Washington, R. N. Kularatne, M. C. Biewer and M. C. Stefan, *ACS Biomater. Sci. Eng.*, 2018, **4**, 997–1004.
- 75 M. L. Bruschi, *Strategies to Modify the Drug Release from Pharmaceutical Systems*, Elsevier, 2015, pp. 63–86.
- 76 R. J. Sandeep Kumar and S. Neeti Nema, *J. Nanomed. Nanotechnol.*, 2015, **6**, 1000317.
- 77 N. S. Heredia, K. Vizuete, M. Flores-Calero, K. Pazmiño, V. F. Pilaquinga, B. Kumar and A. Debut, *PLoS One*, 2022, **17**, e0264825.
- 78 S. Bohrey, V. Chourasiya and A. Pandey, *Nano Convergence*, 2016, **3**, 3.
- 79 H. Li, Y. Zhang, L. Liang, J. Song, Z. Wei, S. Yang, Y. Ma, W. R. Chen, C. Lu and L. Wen, *Materials*, 2022, **15**, 1096.
- 80 Z. Gharehdaghi, R. Rahimi, S. M. Naghib and F. Molaabasi, *J. Iran. Chem. Soc.*, 2022, **19**, 2727–2737.
- 81 A. A. El-Bindary, E. A. Toson, K. R. Shoueir, H. A. Aljohani and M. M. Abo-Ser, *Appl. Organomet. Chem.*, 2020, **34**, e5905.
- 82 I. B. Vasconcelos, T. G. da Silva, G. C. G. Militão, T. A. Soares, N. M. Rodrigues, M. O. Rodrigues, N. B. da Costa, R. O. Freire and S. A. Junior, *RSC Adv.*, 2012, **2**, 9437.